

Efficient Test-Time Adaptation through Latent Subspace Coefficients Search

Xinyu Luo¹ Jie Liu¹ Kecheng Chen¹ Junyi Yang¹ Bo Ding¹ Arindam Basu¹ Haoliang Li¹

Abstract

Real-world deployment often exposes models to distribution shifts, making test-time adaptation (TTA) critical for robustness. Yet most TTA methods are unfriendly to edge deployment, as they rely on backpropagation, activation buffering, or test-time mini-batches, leading to high latency and memory overhead. We propose **ELaTTA** (*Efficient Latent Test-Time Adaptation*), a gradient-free framework for single-instance TTA under strict on-device constraints. ELaTTA freezes model weights and adapts each test sample by optimizing a low-dimensional coefficient vector in a source-induced principal latent subspace, pre-computed offline via truncated SVD and stored with negligible overhead. At inference, ELaTTA encourages prediction confidence by optimizing the k -D coefficients with CMA-ES, effectively optimizing a Gaussian-smoothed objective and improving stability near decision boundaries. Across six benchmarks and multiple architectures, ELaTTA achieves state-of-the-art accuracy under both strict and continual single-instance protocols, while reducing compute by up to $63\times$ and peak memory by $11\times$. We further demonstrate on-device deployment on a ZYNQ-7020 platform. Code will be released upon acceptance.

1. Introduction

The heterogeneity of data in real-world applications poses a significant challenge for modern machine learning systems. During deployment, the data encountered (*a.k.a.* target domain) often deviates from the training data (*a.k.a.* source domain), resulting in out-of-distribution (OOD) data (Recht et al., 2019; Hendrycks & Dietterich, 2019; Hendrycks et al., 2021). This distribution shift undermines the assumption of identical training and test distributions, causing models to struggle in generalizing effectively. OOD scenarios are

¹Department of Electrical Engineering, City University of Hong Kong, Kowloon Tong, Hong Kong SAR. Correspondence to: Haoliang Li <haoliali@cityu.edu.hk>.

Preprint. January 30, 2026.

particularly common in dynamic environments, where deployment conditions, sensor noise, and user behaviors vary significantly. Test-time adaptation (TTA) (Sun et al., 2020; Darestani et al., 2022; Liang et al., 2025) has emerged as a promising solution, allowing models to adapt dynamically to OOD data during inference, which is critical for ensuring robust and reliable AI systems in real-world settings.

TTA is particularly relevant for on-device and edge deployment, where models are embedded in safety and privacy critical pipelines such as mobile authentication, in-vehicle perception, and voice assistant wake-up (Li et al., 2024; Yang et al., 2025). In such scenarios, adaptation often has to be performed locally, where offloading data to the cloud for retraining or continual updates can be impractical due to latency, bandwidth, reliability, and privacy constraints. However, edge platforms operate under tight memory, compute, and energy budgets, which can conflict with common TTA assumptions such as backpropagation and large activation buffers. This motivates TTA methods that are resource-efficient and reliable under strict on-device constraints.

A large body of TTA methods performs *gradient-based optimization* to adjust parameters during inference. Representative methods include TENT (Wang et al., 2021), EATA (Niu et al., 2022), and related objectives based on pseudo-labeling or test-time augmentation consistency (Liang et al., 2020; Zhang et al., 2022; Luo et al., 2025). While effective in many scenarios, these approaches typically require one or multiple gradient steps per test input, which entails backpropagation and storing intermediate activations. Under strict on-device budgets, this optimization pipeline can substantially increase memory footprint and latency, and often becomes the main deployment bottleneck even when only a small subset of parameters is updated. Recent works attempt to reduce this overhead (Hong et al., 2023; Song et al., 2023; Lee et al., 2024; Ma et al., 2025), yet the reliance on gradient computation and activation buffering remains a fundamental friction with resource-limited edge deployment.

Gradient-free TTA is appealing for deployment, but many approaches still require batch statistics (e.g., BN-based adaptation (Schneider et al., 2020; Lim et al., 2023) or batch calibration (Boudiaf et al., 2022)), which is problematic when **edge inputs arrive sequentially and mini-batching via input buffering can be costly in latency and memory**.

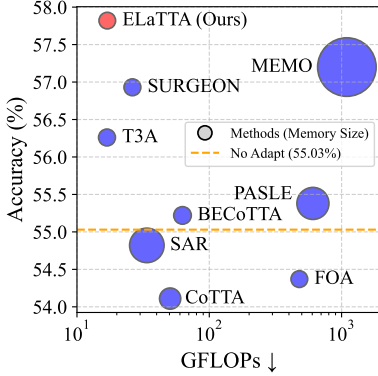


Figure 1. Accuracy, computation, and peak memory comparison of various TTA methods under the single-instance setting on ImageNet-C with ViT-Base model.

In this context, single-instance TTA is commonly considered in two modes: *strict single-instance* adaptation treats each test sample independently (typically without using past samples), whereas *continual single-instance* adaptation operates on a stream and allows updating with information accumulated from previous test inputs. While methods like T3A (Iwasawa & Matsuo, 2021) avoid batch dependency by adjusting the classifier directly, they perform suboptimally under both modes. FOA (Niu et al., 2024) is forward-only but tied to prompt-based models. We thus seek gradient-free, efficient TTA that supports both strict and continual single-instance adaptation without test-time batching, and generalizes across architectures.

To bridge this gap, we propose Efficient Latent Test-Time Adaptation (ELaTTA), a gradient-free TTA method for edge deployment. The key idea is to avoid weight updates and instead *smooth and minimize* test-time entropy by *distributional search* over a few latent coefficients in a source-derived principal subspace. ELaTTA pre-computes a latent principal basis via SVD on a tiny cache of source latents (e.g., 20 samples suffice even at ImageNet scale) and stores it on device with negligible overhead ($\approx 0.01\%$ of backbone parameters). At test time, each input is adapted by optimizing only a compact k -D coefficient vector in this subspace with a forward-only objective, while keeping all network weights fixed. We solve this latent search with CMA-ES (Hansen, 2016), which maintains a Gaussian search distribution and yields covariance-adaptive updates that approximate natural-gradient steps on the resulting Gaussian-smoothed entropy objective. The same procedure supports both *strict* and *continual* single-instance modes, without batching, backpropagation, or activation buffering.

Our main contributions are as follows:

1) **Latent subspace coefficients TTA.** We introduce a non-trivial adaptation paradigm that shifts TTA from high-dimensional weight updates to a *low-dimensional* latent subspace search, adapting only a handful of coefficients per test

input. This paradigm decouples the adaptation complexity from the backbone size, effectively mitigating catastrophic forgetting while maintaining high robustness (see Figure 1), and making it well suited for edge deployment.

2) **Smoothed-entropy optimization via distributional search.** We optimize a *Gaussian-smoothed* entropy objective in the latent subspace to mitigate boundary-induced flips and confirmation bias *without auxiliary losses or gradients*. CMA-ES yields a forward-only, covariance-adaptive approximation to natural-gradient descent on the smoothed risk (see Section 3.3).

3) **Efficiency and broad applicability.** We evaluate ELaTTA on six datasets with substantial real-world distribution shifts under different single-instance protocols. Across model architectures, ELaTTA achieves state-of-the-art accuracy while reducing compute by up to **63 \times** and memory by **11 \times** compared to standard TTA baselines. More importantly, we demonstrate ELaTTA on *ZYNQ-7020 platform*, confirming its practical on-device deployability.

2. Related Work

Single-Instance TTA. Single-instance TTA adapts to distribution shifts when only one test sample is available, making reliable batch statistics (e.g., for BN) difficult to obtain. A common strategy is to construct a pseudo-batch via diverse augmentations, as in SITA (Khurana et al., 2021), DUA (Mirza et al., 2022), MEMO (Zhang et al., 2022), and SPACE (Luo et al., 2025). SITA and DUA primarily update normalization statistics or parameters, whereas MEMO and SPACE optimize the model using consistency objectives in prediction or latent space. Despite their effectiveness, augmentation-based pseudo-batches increase compute and latency, and methods that require backpropagation are less suitable for resource-constrained edge deployment.

Gradient-Free TTA. Gradient-free TTA avoids backpropagation, improving efficiency and suitability for resource-limited devices. Early work mainly recalibrates BN statistics from test data (Schneider et al., 2020), but typically requires multiple samples and is thus less applicable to single-instance settings. Subsequent methods target single-sample adaptation via normalization-centric updates (e.g., SITA (Khurana et al., 2021), mix-up training (Hu et al., 2021), and instance-specific BN adjustment (Gong et al., 2022)). Beyond BN, gradient-free alternatives include prototype-based classifier adaptation (Iwasawa & Matsuo, 2021) and logit-level correction (Boudiaf et al., 2022). However, many gradient-free approaches have limited adaptation capacity because they leave the backbone weights unchanged, motivating methods that better trade off efficiency and effectiveness under large shifts.

Latent Representation Modification for TTA. Latent-

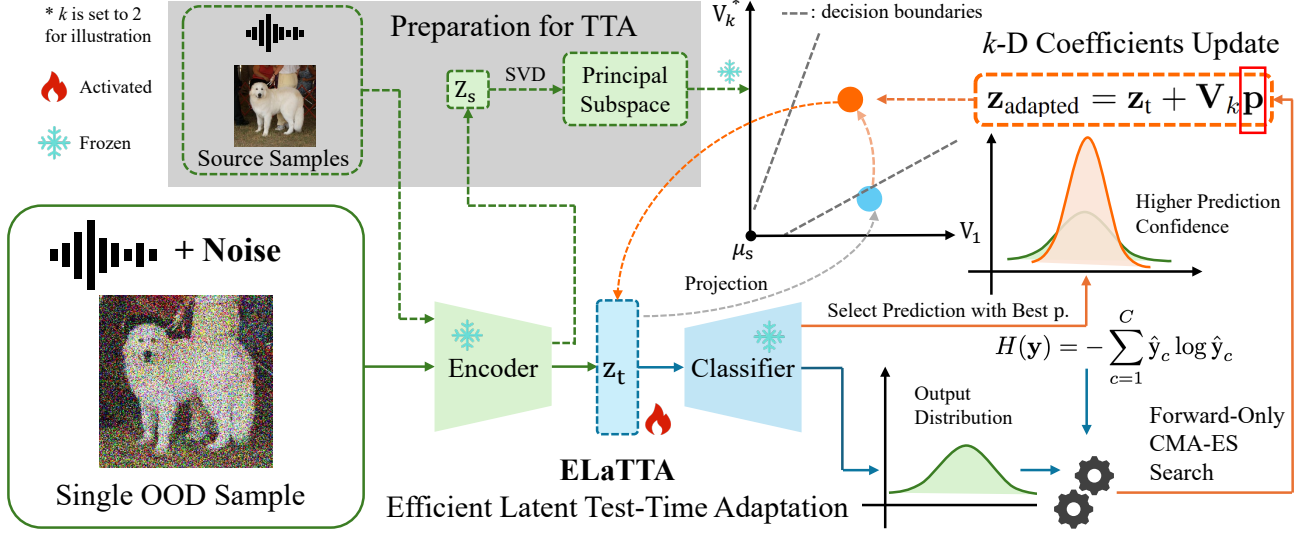


Figure 2. Overview of ELaTTA framework. During offline preparation, we compute a k -dimensional latent PC basis \mathbf{V}_k from source-domain latents. At test time, for a single OOD sample, we perform forward-only adaptation by searching a low-dimensional coefficient $\mathbf{p} \in \mathbb{R}^k$ within the source-induced subspace $\text{span}(\mathbf{V}_k)$ and selecting the update that minimizes prediction entropy. We use CMA-ES for gradient-free optimization, enabling efficient test-time adaptation without backpropagation on edge devices.

space manipulation is widely used in image compression (Djelouah & Schroers, 2019; Shen et al., 2023) and generative modeling (Shen et al., 2020; Vahdat et al., 2021), but is less explored for TTA. A notable exception is Chen et al.’s work (2025), which refines latents for medical image segmentation using a latent CRF loss. While effective, it relies on backpropagation and is task-specific, limiting practicality for resource-constrained and general-purpose deployment. This gap motivates lightweight TTA methods that adapt by modifying latent representations efficiently.

3. Methodology

3.1. Problem Setting and Design Goals

TTA improves robustness under distribution shift, but many existing approaches are difficult to deploy on edge devices, which often require backpropagation with activation buffering, rely on test-time mini-batches, or update many parameters, leading to high memory/latency and potential instability. In this work, we focus on a more *practical single-instance* TTA setting under strict resource constraints, with tight per-sample compute and latency budgets. Our goal is therefore to enable lightweight per-sample adaptation using only forward passes while keeping model weights fixed.

Notation. We consider a model $f = \text{Cls} \circ \text{Enc}$, where $\text{Enc} : \mathcal{X} \rightarrow \mathbb{R}^D$ is a feature extractor (e.g., DNN backbones) mapping an input $\mathbf{x} \in \mathcal{X}$ to a latent representation $\mathbf{z} := \text{Enc}(\mathbf{x}) \in \mathbb{R}^D$, and $\text{Cls} : \mathbb{R}^D \rightarrow \mathcal{Y}$ denotes a prediction classifier head (e.g., a fully connected layer), where D is the latent feature dimension. The model output is $\hat{\mathbf{y}} := \text{Cls}(\mathbf{z})$.

3.2. ELaTTA: Latent Subspace Coefficients Adaptation

Overview. ELaTTA is a single-instance, gradient-free TTA framework designed for edge deployment. Instead of updating network weights which incurs backpropagation, activation buffering, and potential forgetting, ELaTTA adapts each test sample by *searching a few latent coefficients* in a *source-derived principal subspace*. This turns brittle pointwise entropy minimization into a *neighborhood-smoothed* (Gaussian-averaged) objective, yielding stable forward-only adaptation with negligible on-device state.

As illustrated in Figure 2, we first extract a k -dimensional principal basis $\mathbf{V}_k \in \mathbb{R}^{D \times k}$ from a small cache of source latents. At test time, given $\mathbf{z}_t = \text{Enc}(\mathbf{x}_t)$, we optimize a compact coefficient vector $\mathbf{p} \in \mathbb{R}^k$ with a gradient-free solver under a label-free objective, and adapt the latent as

$$\mathbf{z}_{\text{adapted}} = \mathbf{z}_t + \mathbf{V}_k \mathbf{p}. \quad (1)$$

We then predict $\hat{\mathbf{y}} = \text{Cls}(\mathbf{z}_{\text{adapted}})$.

Offline Preparation: Latent Subspace Construction. We build a compact latent subspace from source-domain features. Given random N source samples, we extract their latents and stack them as a matrix $\mathbf{Z}_s \in \mathbb{R}^{N \times D}$, where each row is a latent representation vector. We compute the source mean μ_s , and form the centered feature matrix $\tilde{\mathbf{Z}}_s$. We then compute a rank- k truncated SVD $\tilde{\mathbf{Z}}_s \approx \mathbf{U}_k \mathbf{\Sigma}_k^{(\mathbf{z})} \mathbf{V}_k^\top$, where $\mathbf{V}_k \in \mathbb{R}^{D \times k}$ has orthonormal columns and spans the k -dimensional principal subspace capturing the dominant source variations (with $k \ll D$). We cache \mathbf{V}_k for the following TTA process, and the classifier is expected to be most reliable for latents that can be well represented by this

Algorithm 1 ELaTTA with k Latent Subspace Coefficients

Input: Single test sample \mathbf{x} , encoder Enc , classifier Cls , latent PC basis \mathbf{V}_k , No. of iteration n .
Output: Prediction $\hat{\mathbf{y}}^*$.

Step 1: Generate latent representation.
 Obtain latent \mathbf{z}_t by passing \mathbf{x} through Enc : $\mathbf{z}_t = \text{Enc}(\mathbf{x})$.

Step 2: Optimize latent adaptation.
 Initialize CMA-ES with $\mathbf{m}^{(0)} \leftarrow \mathbf{0}$ (strict single-instance) / \mathbf{p}_{prev} (continual single-instance).
for $t = 1$ **to** n **do**
Sampling: Generate λ candidate solutions.
Evaluation: For each candidate $\mathbf{p}^{(t)}$, compute $\mathbf{z}_{\text{adapted}}$ by Equation (1). Obtain the output $\hat{\mathbf{y}} = \text{Cls}(\mathbf{z}_{\text{adapted}})$ and compute the fitness via Shannon entropy.
Update: Adapt CMA-ES internal parameters based on the top-performing candidates.
end for

Step 3: Return the final prediction.
 Return the \mathbf{p}^* with the smallest fitness value and corresponding output $\hat{\mathbf{y}}^*$.

source-induced subspace. In practice, we find that only a small number of source samples is sufficient to estimate this subspace. For ImageNet-scale settings, $N = 20$ already works well (see Section D.3).

Entropy-Based Test-Time Objective. At test time, ground-truth labels are unavailable. We therefore adopt Shannon entropy (Shannon, 1948) minimization as a standard self-supervised objective to encourage confident predictions (Grandvalet & Bengio, 2004; Wang et al., 2021; Zhang et al., 2022; Chen et al., 2025) given as $H(\hat{\mathbf{y}}) \triangleq -\sum_{c=1}^C \hat{y}_c \log \hat{y}_c$, where \hat{y}_c denotes the predicted probability of class c , and C is the total number of classes.

Crucially, our adaptation does not update network parameters. Instead, we search for a *low-dimensional* latent coefficients $\mathbf{p} \in \mathbb{R}^k$ within the subspace \mathbf{V}_k . Using the adaptation form in Equation (1), we obtain an adapted latent $\mathbf{z}_{\text{adapted}}$ and the corresponding prediction. A straightforward test-time objective is to minimize the *pointwise* entropy as

$$\min_{\mathbf{p} \in \mathbb{R}^k} \mathcal{L}(\mathbf{p}) \quad \text{where} \quad \mathcal{L}(\mathbf{p}) \triangleq H(\text{Cls}(\mathbf{z}_t + \mathbf{V}_k \mathbf{p})). \quad (2)$$

This formulation highlights a key design choice of ELaTTA. We restrict adaptation to $\text{span}(\mathbf{V}_k)$, which not only bounds the degrees of freedom of per-sample updates but also prevents unconstrained drift in latent directions unsupported by the source representation.

Pointwise Entropy Can Be Brittle. Despite its simplicity, minimizing $\mathcal{L}(\mathbf{p})$ pointwise can be unstable when the test latent \mathbf{z}_t lies close to a decision boundary. Even small corruptions can flip the top-1 class, introducing *noise-induced decision flips*. In this regime, any strictly local optimization

(e.g., pointwise entropy minimization) tends to over-commit to the currently dominant prediction, which may be incorrect, thereby exhibiting confirmation bias. This is particularly problematic in single-instance, label-free TTA where we cannot rely on batch statistics, temporal ensembling, or additional supervision to correct early mis-commitments.

Distribution-Smoothed Entropy Objective. To stabilize adaptation *without* introducing auxiliary losses or back-propagated gradients, we optimize a *neighborhood-robust* objective obtained by Gaussian smoothing in the coefficient space. Specifically, we maintain a search distribution $\mathbf{p} \sim \mathcal{N}(\mathbf{m}, \Sigma)$ and minimize the smoothed objective $\min_{\mathbf{m}, \Sigma \succ 0} J(\mathbf{m}, \Sigma)$, where

$$J(\mathbf{m}, \Sigma) \triangleq \mathbb{E}_{\mathbf{p} \sim \mathcal{N}(\mathbf{m}, \Sigma)} [H(\text{Cls}(\mathbf{z}_t + \mathbf{V}_k \mathbf{p}))]. \quad (3)$$

Unlike the pointwise objective $\mathcal{L}(\mathbf{p})$, minimizing J encourages low entropy *not only at a single point* but throughout a neighborhood of \mathbf{m} . Since predictions are most unstable near decision boundaries, this neighborhood-averaged criterion biases the search toward regions where the classifier is locally consistent with larger effective margins, thereby reducing decision flips and mitigating confirmation bias.

Gradient-Free Distributional Search via CMA-ES. We optimize Equation (3) using CMA-ES, a gradient-free optimizer for continuous black-box objectives. Importantly, CMA-ES is not used here as a generic “replacement for gradients” on $\mathcal{L}(\mathbf{p})$. Rather, it directly operates on the *search distribution* $\mathcal{N}(\mathbf{m}, \Sigma)$, making it well matched to the distribution-smoothed objective $J(\mathbf{m}, \Sigma)$.

Given a per-sample budget of n iterations and a fixed population size λ per iteration, CMA-ES proceeds iteratively by sampling candidate coefficients $\{\mathbf{p}_i\}$ from the current Gaussian $\mathcal{N}(\mathbf{m}, \Sigma)$, evaluating their fitness via forward passes using $\mathcal{L}(\mathbf{p}_i)$, and then updating (\mathbf{m}, Σ) according to the ranked candidates. This procedure requires no backpropagation and does not modify any network parameters.

Across all evaluated candidates during the n iterations, we keep the best coefficient $\mathbf{p}^* \triangleq \arg \min_{\mathbf{p} \in \mathcal{S}} \mathcal{L}(\mathbf{p})$, where \mathcal{S} denotes the set of all sampled coefficients. We then form the adapted latent via Equation (1) and output the corresponding prediction. This best-sample rule is simple, budget-aware, and aligns with the goal of finding a high-confidence prediction within the source-induced feasible set. The overall algorithm is shown in Algorithm 1.

3.3. Theoretical Analysis

We provide a theoretical justification for ELaTTA from two perspectives: subspace-constrained latent adaptation and distribution smoothing induced by CMA-ES in the latent coefficient space.

Effect of Subspace-Constrained Latent Adaptation. Let $\mathbf{z}^* \in \mathbb{R}^D$ be the clean latent feature and $\mathbf{z}_t = \mathbf{z}^* + \boldsymbol{\xi}$ the corrupted one. Let $\mathbf{V}_k \in \mathbb{R}^{D \times k}$ have orthonormal columns spanning the principal subspace, and define the orthogonal projector onto $\text{span}(\mathbf{V}_k)$ as $\mathbf{P} = \mathbf{V}_k \mathbf{V}_k^\top$. Decompose $\boldsymbol{\xi} = \boldsymbol{\xi}_{\parallel} + \boldsymbol{\xi}_{\perp}$ with $\boldsymbol{\xi}_{\parallel} = \mathbf{P}\boldsymbol{\xi}$ and $\boldsymbol{\xi}_{\perp} = (\mathbf{I} - \mathbf{P})\boldsymbol{\xi}$ (Golub & Van Loan, 2013; Horn & Johnson, 2012). We adapt within the subspace via Equation (1).

Proposition 3.1 (Subspace-Constrained Error Decomposition). *For $\mathbf{z}_{\text{adapted}} = \mathbf{z}_t + \mathbf{V}_k \mathbf{p}$,*

$$\|\mathbf{z}_{\text{adapted}} - \mathbf{z}^*\|^2 = \|\boldsymbol{\xi}_{\parallel} + \mathbf{V}_k \mathbf{p}\|^2 + \|\boldsymbol{\xi}_{\perp}\|^2. \quad (4)$$

Consequently, adaptation in $\text{span}(\mathbf{V}_k)$ cannot introduce any update in $\text{span}(\mathbf{V}_k)^\perp$.

Proposition 3.1 formalizes ELaTTA’s bounded degrees-of-freedom property. The orthogonal corruption component $\boldsymbol{\xi}_{\perp}$ is independent of \mathbf{p} , so latent updates are confined to a controlled k -dimensional subspace.

Distribution Smoothing in Coefficient Space. Recall the smoothed objective $J(\mathbf{m}, \boldsymbol{\Sigma})$ in Equation (3), where $\mathcal{L}(\mathbf{p})$ is defined in Equation (2).

Proposition 3.2 (Score-function gradient and induced rank- k smoothing). *Let $J(\mathbf{m}, \boldsymbol{\Sigma}) = \mathbb{E}_{\mathbf{p} \sim \mathcal{N}(\mathbf{m}, \boldsymbol{\Sigma})}[\mathcal{L}(\mathbf{p})]$. The gradient with respect to the mean satisfies*

$$\nabla_{\mathbf{m}} J(\mathbf{m}, \boldsymbol{\Sigma}) = \mathbb{E}_{\mathbf{p} \sim \mathcal{N}(\mathbf{m}, \boldsymbol{\Sigma})} \left[\mathcal{L}(\mathbf{p}) \boldsymbol{\Sigma}^{-1} (\mathbf{p} - \mathbf{m}) \right]. \quad (5)$$

Moreover, sampling \mathbf{p} induces $\mathbf{z}(\mathbf{p}) = \mathbf{z}_t + \mathbf{V}_k \mathbf{p} \sim \mathcal{N}(\mathbf{z}_t + \mathbf{V}_k \mathbf{m}, \mathbf{V}_k \boldsymbol{\Sigma} \mathbf{V}_k^\top)$, whose covariance is rank- k .

Proposition 3.2 makes explicit that optimizing $(\mathbf{m}, \boldsymbol{\Sigma})$ corresponds to descending a Gaussian-smoothed loss in coefficient space, while the induced smoothing in latent space is confined to $\text{span}(\mathbf{V}_k)$. We optimize this objective using CMA-ES as described in Section 3.2.

Detailed proofs and derivations are provided in Section B.

3.4. Complexity & Deployment Notes

Offline statistic & storage. The subspace basis $\mathbf{V}_k \in \mathbb{R}^{D \times k}$ is computed *once* offline from tens of source latents and then kept fixed during deployment. Adaptation process does not require accessing any source samples. In this sense, \mathbf{V}_k is a compact deployment-time statistic (similar in spirit to BN running statistics). For ImageNet with ViT-B, storing \mathbf{V}_k costs $\approx 0.05\text{MB}$ while the model size is $\approx 330.28\text{MB}$, i.e., $\frac{0.05}{330.28} \times 100\% \approx 0.015\% (< 0.02\%)$, which is negligible in practice.

Online overhead. The dominant runtime cost comes from black-box objective evaluations in CMA-ES. With population size λ and n iterations, ELaTTA performs $E = \lambda n$

evaluations per test sample. Note that the backbone is executed only *once* to obtain and cache \mathbf{z}_t . CMA-ES then re-evaluates only the lightweight classifier E times (rather than E full-model forward passes). Consequently, the FLOPs scale as $F_{\text{Enc}} + E F_{\text{Cls}}$, where F_{Enc} and F_{Cls} denotes the FLOPs of one encoder and classifier forward pass respectively. The additional cost $\approx (E - 1)F_{\text{Cls}}$ is typically small when $F_{\text{Cls}} \ll F_{\text{Enc}}$. The remaining arithmetic is light. Forming $\mathbf{z}_{\text{adapted}}$ costs $\mathcal{O}(Dk)$ per evaluation (thus $\mathcal{O}(EDk)$ total) and CMA-ES bookkeeping costs at most $\mathcal{O}(Ek^2)$. Candidate evaluations are embarrassingly parallel and can be batched on accelerators to reduce wall-clock latency. We report and analyze empirical wall-clock latency and peak memory in Section 4.3.

Quantized variants. To further reduce numerical and memory overhead, Section C studies two quantized variants that represent the adapted parameters $\mathbf{p} \in \mathbb{R}^k$ using fewer numerical levels and, when applicable, runs the CMA-ES procedure in fixed-point arithmetic. We report the corresponding accuracy trade-offs.

4. Experiments

4.1. Experimental Setup

Single-instance protocols. We consider two practical single-instance TTA protocols: (1) *strict single-instance* TTA, where each test input is adapted *independently* and the model/state is reset after every sample; and (2) *continual single-instance* TTA, where test samples arrive as a stream and adaptation may leverage information accumulated from previous inputs. Unless otherwise specified, all main results use the *strict* protocol with batch size 1. Continual results are reported in Section D.

Tasks, datasets, and models. We evaluate ELaTTA on image classification (IC) and keyword spotting (KWS). For IC, we use four ImageNet-based OOD benchmarks namely ImageNet-C (Hendrycks & Dietterich, 2019), ImageNet-V2 (Recht et al., 2019), ImageNet-R (Hendrycks et al., 2021), and ImageNet-Sketch (Wang et al., 2019). We additionally evaluate on DomainNet-126, a 126-class subset of DomainNet (Peng et al., 2019), to assess robustness under larger domain shifts; results are reported in Section D. We adopt ViT-Base (Dosovitskiy et al., 2021) pretrained on ImageNet-1k (Russakovsky et al., 2015) as the source model for the ImageNet-based benchmarks. For KWS, we construct GSC-C by mixing Google Speech Commands (GSC) (Warden, 2018) with real-world background noise from ESC-50 (Piczak, 2015) at varying SNRs, and use a pretrained LSTM (Yang et al., 2025) trained on clean GSC as the source model. We report **classification accuracy** (%), \uparrow on OOD test samples.

Baselines. We compare against both *gradient-free* and

Table 1. Performance comparison on ImageNet-C with ViT-Base model regarding **Accuracy** (%). GF stands for gradient-free. The **bold** number indicates the best result.

Method	GF	Gauss.	Noise		Blur			Weather			Digital			Average Acc.			
			Shot	Impl.	Defoc.	Glass	Motion	Zoom	Snow	Frost	Fog	Brit.	Contr.	Elas.	JPEG		
No Adapt	✓	55.34	56.23	56.01	46.48	34.78	52.87	44.20	62.39	62.66	65.56	77.70	32.04	45.73	66.72	66.67	55.03
FOA (ICML'24)	✓	53.87	54.16	54.00	46.17	33.45	52.56	43.69	61.82	62.30	66.17	77.73	30.60	46.14	66.18	66.77	54.37
T3A (NeurIPS'21)	✓	54.69	55.95	55.61	47.41	36.77	53.91	46.44	63.85	60.42	68.12	78.11	37.79	49.54	67.24	68.04	56.26
CoTTA (CVPR'22)	✗	54.61	55.66	55.37	45.28	34.35	52.69	44.11	62.38	62.62	58.33	77.71	29.58	45.65	66.68	66.66	54.11
SAR (ICLR'23)	✗	55.25	56.08	55.89	46.22	34.41	52.28	43.82	62.09	62.69	65.56	77.53	32.03	45.47	66.37	66.55	54.82
PASLE (ICLR'25)	✗	56.72	56.24	56.21	47.53	35.32	53.02	44.03	62.43	62.81	65.84	78.62	31.23	46.65	66.76	67.24	55.38
BECoTTA (ICML'24)	✗	55.67	56.45	56.29	46.21	33.68	52.66	43.67	62.20	63.37	68.25	77.58	33.74	45.09	66.70	66.78	55.22
SURGEON (CVPR'25)	✗	58.70	59.22	59.23	48.82	35.29	55.06	45.87	64.83	65.94	61.76	79.56	34.46	46.90	69.02	69.36	56.93
MEMO (NeurIPS'22)	✗	55.90	54.20	56.30	45.79	39.34	53.02	45.13	42.56	47.82	65.31	80.01	69.63	49.21	69.51	71.33	56.34
ELaTTA (ours)	✓	58.77	59.66	59.50	49.30	36.08	55.35	46.34	65.21	66.40	67.66	80.21	35.96	47.61	69.55	69.68	57.82

Table 2. Performance comparison on ImageNet-C with ViT-Base model regarding **Accuracy** (%). GF stands for gradient-free. The **bold** number indicates the best result.

Method	GF	Accuracy (%)				Avg.
		V2	R	Sketch	Avg.	
No Adapt	✓	75.49	59.49	44.89	59.96	
FOA (ICML'24)	✓	75.25	59.96	44.95	60.05	
T3A (NeurIPS'21)	✓	75.61	57.98	48.44	60.68	
CoTTA (CVPR'22)	✗	75.50	59.20	44.77	59.82	
SAR (ICLR'23)	✗	75.33	59.39	44.82	59.85	
PASLE (ICLR'25)	✗	75.66	61.73	45.72	61.04	
MEMO (NeurIPS'22)	✗	76.08	62.85	46.08	61.67	
ELaTTA(ours)	✓	78.15	65.29	47.73	63.72	

gradient-based TTA methods, as well as No Adapt. Gradient-free baselines include T3A (Iwasawa & Matsuo, 2021) and FOA (Niu et al., 2024). Gradient-based baselines include CoTTA (Wang et al., 2022), MEMO (Zhang et al., 2022), SAR (Niu et al., 2023), PASLE (Hu et al., 2025), BECoTTA (Lee et al., 2024), and SURGEON (Ma et al., 2025). For fair comparison under the strict single-instance protocol, we set the test-time batch size to 1 for all baselines and reset the model/state after each test sample whenever applicable. All baselines are reproduced with official implementations and recommended hyperparameters unless explicitly stated.

Implementation details of ELaTTA. ELaTTA adapts each test sample by optimizing a low-dimensional coefficient vector $\mathbf{p} \in \mathbb{R}^k$ in a pre-computed latent principal subspace while keeping all network weights frozen. We set $k = 16$ for IC and $k = 2$ for KWS unless otherwise specified. We compute the subspace basis \mathbf{V}_k offline via truncated SVD on source latents and cache \mathbf{V}_k for deployment; no source samples are accessed at test time. For CMA-ES (Hansen, 2016), the population size is set to $\lambda = 4 + 3 \log(k)$ and the number of iterations is $n = 8$ for IC and $n = 2$ for KWS. Additional experimental details are provided in Section D.

4.2. Main Results and Analyses

In this section, we evaluate our proposed ELaTTA method on two tasks, IC and KWS, and compare it with state-of-

the-art TTA methods. The primary focus is to assess the effectiveness of our method in handling distribution shifts, while maintaining efficiency and stability during TTA. The results highlight the superior performance of our approach across diverse datasets and tasks.

Performance Comparison on Image Classification. We evaluate ELaTTA on ImageNet-C with ViT-Base under the *strict single-instance* protocol. As shown in Table 1, ELaTTA achieves the best average accuracy of 57.82% and delivers strong performance across most corruption types, indicating robust adaptation under diverse shifts. Under this strict setting, methods that depend on batch/stream statistics or stabilized pseudo-targets tend to be less effective. FOA benefits from richer test-time context, CoTTA’s EMA teacher can be noisy when updated from single-sample pseudo-labels, and SAR’s reliable-sample selection and sharpness-aware updates are difficult to realize with batch-1 inputs. History-based methods such as T3A are also disadvantaged because their support-set updates make predictions order-dependent; enforcing per-instance independence largely weakens the adaptation signal. Finally, PASLE provides modest but consistent gains via selective pseudo-labeling, while gradient-based single-sample adaptation MEMO face challenges due to instability and catastrophic forgetting since it updates the whole weights of the model. Overall, ELaTTA offers the strongest accuracy and stability without backpropagation.

Beyond ImageNet-C, Table 2 shows that ELaTTA also achieves the best average accuracy (63.72%) on ImageNet-V2, ImageNet-R, and ImageNet-Sketch, consistently outperforming all baselines. These results further validate the effectiveness of ELaTTA under diverse distribution shifts.

Performance Comparison on Keyword Spotting. We omit CoTTA and MEMO since they rely on image-style augmentations and their speech-time counterparts require additional design choices, and FOA since it is prompt-based and not compatible with our LSTM KWS backbone. We therefore compare ELaTTA with T3A, SAR, and PASLE on GSC-C under SNR of -10/-15/-20 dB (Table 3). ELaTTA

Table 3. Performance comparison on GSC-C with LSTM model regarding **Accuracy (%)**. GF stands for gradient-free. The **bold** number indicates the best result.

SNR	Method	GF	Animals		Natural		Human		Domestic		Urban		Average Acc.
			dog	cat	pouringwater	thunderstorm	cryingbaby	laughing	washingmachine	vacuumcleaner	carhorn	fireworks	
-10 dB	No Adapt	✓	62.67	61.17	54.55	66.23	58.74	58.59	52.88	50.43	56.62	61.54	58.34
	T3A (NeurIPS'21)	✓	62.67	61.17	54.55	66.23	58.74	58.59	52.88	50.43	56.62	61.54	58.34
	SAR (ICLR'23)	✗	61.33	59.85	52.79	63.92	55.80	56.95	49.53	47.31	55.06	60.21	56.28
	PASLE (ICLR'25)	✗	62.87	62.06	54.78	66.75	59.42	59.63	57.69	53.38	58.35	62.73	59.77
-15 dB	ELaTTA (ours)	✓	64.25	63.58	59.73	66.47	61.99	61.94	59.46	56.98	59.32	64.90	61.86
	No Adapt	✓	57.08	53.63	49.35	61.45	53.08	53.03	46.81	47.49	51.76	55.19	52.89
	T3A (NeurIPS'21)	✓	57.08	53.63	49.35	61.45	53.08	53.03	46.81	47.49	51.76	55.19	52.89
	SAR (ICLR'23)	✗	55.33	52.36	47.49	59.35	51.01	50.85	44.13	44.37	50.82	54.13	50.98
-20 dB	PASLE (ICLR'25)	✗	58.12	53.77	52.49	61.93	55.64	56.72	48.34	49.23	52.67	59.32	54.82
	ELaTTA (ours)	✓	60.84	57.99	57.71	62.28	58.04	58.98	57.83	55.38	56.00	60.41	58.55
	No Adapt	✓	52.75	48.50	46.21	58.08	51.12	48.53	45.55	46.05	48.81	50.94	49.65
	T3A (NeurIPS'21)	✓	52.75	48.50	46.21	58.08	51.12	48.53	45.55	46.05	48.81	50.94	49.65
-30 dB	SAR (ICLR'23)	✗	51.28	46.95	44.28	55.51	47.82	46.68	41.45	43.41	48.23	50.10	47.57
	PASLE (ICLR'25)	✗	53.76	51.77	48.84	59.03	53.31	50.38	46.21	50.21	52.17	53.56	51.92
	ELaTTA (ours)	✓	59.07	54.71	57.20	59.35	56.94	57.94	58.22	55.54	54.50	58.07	57.15

Table 4. Performance comparison on ImageNet-C with ViT-Base model using different k and n regarding **Accuracy (%)**. The **bold** number indicates the best result.

$k\{k\}n\{n\}$	k8n2	k8n4	k8n8	k8n10	k16n2	k16n4	k16n8	k16n10	k32n2	k32n4	k32n8	k32n10
Accuracy	55.07	55.39	51.40	50.01	55.12	56.88	57.82	52.44	55.16	55.56	57.22	53.24

Table 5. Performance comparison on ImageNet-C with ViT-Base model regarding **Accuracy (%)**. GF stands for gradient-free. The **bold** number indicates the best result.

Method	GF	GFLOPs	Mem (MB)	Time (s)
FOA (ICML'24)	✓	479.31	702	0.273
T3A (NeurIPS'21)	✓	16.86	718	0.124
CoTTA (CVPR'22)	✗	50.59	1130	0.703
SAR (ICLR'23)	✗	33.73	2996	0.037
PASLE (ICLR'25)	✗	607.13	2588	0.051
MEMO (NeurIPS'22)	✗	1096.14	8632	1.009
BECoTTA (ICML'24)	✗	62.74	778	0.082
SURGEON (CVPR'25)	✗	26.24	716	0.071
ELaTTA(ours)	✓	16.95	696	0.042

consistently achieves the best accuracy, with gains increasing as SNR decreases, indicating that the fixed principal subspace (V_k) provides effective source-domain guidance under heavier noise. In contrast, T3A is close to No Adapt due to insufficient confident per-class supports in the 12-class, single-instance setting, and SAR is largely ineffective on this backbone (no normalization layers to adapt), often reducing to unstable entropy minimization. PASLE yields small but consistent improvements, further underscoring the practical advantage of ELaTTA for noisy KWS.

4.3. Ablation Studies

Effect of Hyperparameters k and n . As shown in Table 4, the choice of k and n presents a trade-off between subspace expressiveness and optimization stability, with $k = 16, n = 8$ achieving the optimal balance. Specifically, k controls the subspace capacity. A small k limits useful variation, while an excessively large k introduces noisy directions and

complicates the search space. Regarding n , it governs the optimization strength. While sufficient steps are needed for adaptation, an overly large n causes the solver to overfit the unsupervised proxy rather than improving generalization, leading to performance degradation.

Analyses of Computational Efficiency. As shown in Figure 1 and Table 5, ELaTTA demonstrates significant advantages in computational complexity compared to other methods. Specifically, ELaTTA achieves a GFLOPs value of 16.95, which is among the lowest across all methods, highlighting its high computational efficiency. T3A suffers from longer runtime despite having the lowest GFLOPs, due to its computation being concentrated in the final linear layer and support set updates, which are difficult to parallelize and fully utilize hardware resources. Additionally, its entropy filtering step, which involves calculating and filtering prediction entropy for each sample, introduces additional overhead when the support set is large. In terms of memory usage, ELaTTA requires only 696 MB, making it the most memory-efficient approach in the comparison. Moreover, ELaTTA achieves a short runtime per sample, at just 0.042 seconds, significantly outperforming other methods such as MEMO (1.009 s) and CoTTA (0.703 s). Gradient-based SAR achieve slightly shorter running time by only updating the affine parameters in normalization layers, thereby reducing the computational cost of parameter updates. However, as shown in Table 1, this strategy struggles in single-sample scenarios, where updating affine parameters alone may not be sufficient to achieve effective TTA.

Effect on Diverse Backbones. We evaluate ELaTTA across ResNet-50 (He et al., 2016), EfficientNet-B0 (Tan & Le,

Table 6. Performance comparison on ImageNet-C with ResNet-50, EfficientNet-B0 and MobileNet-V4 regarding **Accuracy (%)**. The **bold** number indicates the best result.

Networks	Method	Noise		Blur			Weather				Digital			Average Acc.			
		Gauss.	Shot	Impl.	Defoc.	Glass	Motion	Zoom	Snow	Frost	Fog	Brit.	Contr.	Elas.	Pix.	JPEG	
ResNet-50	No Adapt	4.47	4.74	4.06	8.11	5.96	9.59	14.74	6.92	14.47	12.32	45.80	0.72	11.08	18.19	32.54	12.91
	IABN	7.22	5.10	5.54	5.46	7.38	11.92	15.98	5.74	12.32	14.14	47.10	0.90	7.10	18.26	18.04	12.15
	TTN	1.73	5.13	4.90	4.17	6.69	10.16	14.14	6.13	14.52	14.42	49.20	0.22	12.26	22.03	33.07	13.25
	SAR	2.34	4.46	4.24	6.56	6.66	14.04	16.34	4.02	14.68	13.26	48.51	0.35	12.43	20.44	36.46	13.65
	ELaTTA	4.99	5.18	4.41	11.36	7.32	14.26	18.29	7.00	15.32	15.01	55.32	0.25	13.07	23.29	40.97	15.74
EfficientNet-B0	No Adapt	15.07	18.47	14.66	21.48	8.66	21.73	24.24	30.95	27.77	28.80	67.25	21.96	17.62	46.73	50.51	27.73
	IABN	14.71	19.32	14.75	21.34	9.24	21.59	25.65	33.35	29.45	29.56	69.24	22.51	17.88	49.46	53.32	28.76
	TTN	15.32	12.34	15.32	23.44	6.32	23.23	26.36	32.02	28.66	32.74	69.35	24.78	18.50	52.64	54.44	29.03
	SAR	15.34	20.58	16.22	22.53	4.24	20.34	22.35	32.45	20.76	28.63	68.64	22.46	16.34	46.86	49.58	27.15
	ELaTTA	16.61	21.53	16.71	25.02	7.57	25.91	27.69	35.05	30.38	32.78	75.67	25.96	18.50	55.14	59.24	31.58
MobileNet-V4	No Adapt	5.97	7.58	6.02	9.69	3.03	12.30	11.19	12.57	20.20	11.41	58.11	3.84	11.05	10.29	32.79	14.40
	IABN	5.32	7.50	6.23	9.46	3.02	12.34	11.68	12.34	20.68	13.46	66.48	2.02	11.36	9.68	36.46	15.20
	TTN	6.98	7.54	6.38	9.84	3.34	13.56	12.56	12.64	20.46	12.42	64.66	2.46	10.48	10.46	40.58	15.62
	SAR	4.98	7.32	4.54	10.20	3.02	14.54	11.08	12.78	22.34	11.60	60.34	2.66	10.46	11.42	39.64	15.13
	ELaTTA	5.47	7.55	5.43	10.89	2.99	14.57	12.28	13.17	23.08	12.70	68.52	2.78	11.77	11.77	41.43	16.29

Table 7. Evaluation on edge device for KWS task (GSC-C under SNR of -10 dB) with LSTM model regarding **Accuracy (%)**. The **bold** number indicates the best result.

Method	Devices	Animals		Natural			Human		Domestic			Urban		Average Acc.	
		dog	cat	pouringwater	thunderstorm	cryingbaby	laughing	washingmachine	vacuumcleaner	carhorn	fireworks				
No Adapt	RTX 3090	62.67	61.17	54.55	66.23	58.74	58.59	52.88	50.43	56.62	61.54	58.34			
		64.25	63.58	59.73	66.47	61.99	61.94	59.46	56.98	59.32	64.90	61.86 (+3.52)			
No Adapt	ZYNQ 7020	57.03	56.29	50.03	60.74	51.52	52.42	50.75	52.88	54.74	59.19	54.56			
		58.06	57.70	53.04	61.04	53.63	54.31	52.39	54.93	58.18	59.62	56.29 (+1.73)			

2019), MobileNet-V4 (Qin et al., 2024). As all use BN, we include BN-specific baselines IABN (Gong et al., 2022) and TTN (Lim et al., 2023) in Table 6. On ResNet-50, ELaTTA improves accuracy on most domains, yielding a +2.83% gain on average. It also boosts the lightweight EfficientNet-B0 (5.29M) and MobileNet-V4 (3.77M), though gains are limited under extreme corruptions (e.g., Glass Blur on MobileNet-V4, Contrast on ResNet-50) where accuracy is near random (3.03%, 0.72%). This likely reflects catastrophic feature degradation. When semantic signal vanishes, latent-space TTA becomes ineffective, suggesting stronger backbone robustness is required in such regimes.

Demonstration on Edge Device ZYNQ 7020. To assess the *edge deployability* of our TTA framework, we implement ELaTTA on ZYNQ 7020, a widely utilized SoC with an ARM Cortex-A9 processor and FPGA-based programmable logic. This experiment is intended as a *proof-of-concept* rather than a performance benchmark. Our goal is to show that TTA can be executed *on-device* under strict hardware constraints, where gradient-based adaptation is generally impractical due to the need for backpropagation and large activation buffers. In contrast, ELaTTA adapts by updating only a low-dimensional latent vector using forward passes, making it suitable for such resource-constrained settings.

We evaluate the on-device system on the KWS task at SNR of -10 dB. As shown in Table 7, *both* the non-adaptive on-device baseline and the on-device ELaTTA system are implemented using the same 16-bit fixed-point arithmetic

pipeline. Compared to GPU evaluation in 32-bit floating-point (reported as a reference), the reduced numerical precision on ZYNQ 7020 introduces an accuracy gap. Nevertheless, ELaTTA still yields a clear improvement over the non-adaptive on-device baseline, demonstrating robust adaptation and supporting the feasibility of deploying our framework in real-world edge scenarios.

5. Conclusion and Limitation

We presented ELaTTA, an efficient single-instance TTA framework with a low-dimensional latent coefficient search in a source-derived principal subspace, effectively optimizing a Gaussian-smoothed entropy objective while keeping all network weights frozen. Instantiated with forward-only CMA-ES, ELaTTA achieves negligible on-device state, making it practical under tight memory and latency constraints. Across diverse datasets, architectures, and distribution shifts, ELaTTA achieves strong robustness in both *strict* and *continual* single-instance settings while substantially reducing compute and peak memory. We further validate ELaTTA’s deployability via a proof-of-concept implementation on ZYNQ-7020. However, this paper only focuses on the algorithmic design. An exciting next step is algorithm-hardware co-design, including dedicated accelerator modules tailored to ELaTTA’s latent search to further improve end-to-end efficiency on deployed systems.

Impact Statement

This paper presents work whose goal is to advance the field of Machine Learning. There are many potential societal consequences of our work, none which we feel must be specifically highlighted here.

References

Boudiaf, M., Mueller, R., Ben Ayed, I., and Bertinetto, L. Parameter-free online test-time adaptation. In *Proceedings of the IEEE/CVF Conference on Computer Vision and Pattern Recognition*, pp. 8344–8353, 2022.

Chen, K., Luo, X., Qin, T., Liu, J., Liu, H., Lee, V. H. F., Yan, H., and Li, H. Test-time adaptation for foundation medical segmentation model without parametric updates. In *Proceedings of the IEEE/CVF International Conference on Computer Vision*, 2025.

Darestani, M. Z., Liu, J., and Heckel, R. Test-time training can close the natural distribution shift performance gap in deep learning based compressed sensing. In *International conference on machine learning*, pp. 4754–4776. PMLR, 2022.

Deng, Z., Chen, G., Niu, S., Luo, H., Zhang, S., Yang, Y., Chen, R., Luo, W., and Tan, M. Test-time model adaptation for quantized neural networks. In *Proceedings of the 33rd ACM International Conference on Multimedia*, pp. 7258–7267, 2025.

Djelouah, J. and Schroers, C. Content adaptive optimization for neural image compression. In *Proc. IEEE Comput. Soc. Conf. Comput. Vis. Pattern Recognit*, volume 2, pp. 1–5, 2019.

Dosovitskiy, A., Beyer, L., Kolesnikov, A., Weissenborn, D., Zhai, X., Unterthiner, T., Dehghani, M., Minderer, M., Heigold, G., Gelly, S., et al. An image is worth 16x16 words: Transformers for image recognition at scale. In *International Conference on Learning Representations*, 2021.

Golub, G. H. and Van Loan, C. F. *Matrix computations*. JHU press, 2013.

Gong, T., Jeong, J., Kim, T., Kim, Y., Shin, J., and Lee, S.-J. Note: Robust continual test-time adaptation against temporal correlation. *Advances in Neural Information Processing Systems*, 35:27253–27266, 2022.

Grandvalet, Y. and Bengio, Y. Semi-supervised learning by entropy minimization. *Advances in neural information processing systems*, 17, 2004.

Hansen, N. The cma evolution strategy: A tutorial. *arXiv preprint arXiv:1604.00772*, 2016.

He, K., Zhang, X., Ren, S., and Sun, J. Deep residual learning for image recognition. In *Proceedings of the IEEE conference on computer vision and pattern recognition*, pp. 770–778, 2016.

Hendrycks, D. and Dietterich, T. Benchmarking neural network robustness to common corruptions and perturbations. *Proceedings of the International Conference on Learning Representations*, 2019.

Hendrycks, D., Basart, S., Mu, N., Kadavath, S., Wang, F., Dorundo, E., Desai, R., Zhu, T., Parajuli, S., Guo, M., Song, D., Steinhardt, J., and Gilmer, J. The many faces of robustness: A critical analysis of out-of-distribution generalization. *ICCV*, 2021.

Hong, J., Lyu, L., Zhou, J., and Spranger, M. Mecta: Memory-economic continual test-time model adaptation. In *2023 International Conference on Learning Representations*, 2023.

Horn, R. A. and Johnson, C. R. *Matrix analysis*. Cambridge university press, 2012.

Hu, X., Uzunbas, G., Chen, S., Wang, R., Shah, A., Nevaria, R., and Lim, S.-N. Mixnorm: Test-time adaptation through online normalization estimation. *arXiv preprint arXiv:2110.11478*, 2021.

Hu, Y., Qiao, C., Geng, X., and Xu, N. Selective label enhancement learning for test-time adaptation. In *The Thirteenth International Conference on Learning Representations*, 2025.

Iwasawa, Y. and Matsuo, Y. Test-time classifier adjustment module for model-agnostic domain generalization. *Advances in Neural Information Processing Systems*, 34: 2427–2440, 2021.

Khurana, A., Paul, S., Rai, P., Biswas, S., and Aggarwal, G. Sita: Single image test-time adaptation. *arXiv preprint arXiv:2112.02355*, 2021.

Lee, D., Yoon, J., and Hwang, S. J. Becotta: Input-dependent online blending of experts for continual test-time adaptation. *arXiv preprint arXiv:2402.08712*, 2024.

Li, X., Li, Y., Li, Y., Cao, T., and Liu, Y. Flexnn: Efficient and adaptive dnn inference on memory-constrained edge devices. In *Proceedings of the 30th Annual International Conference on Mobile Computing and Networking*, pp. 709–723, 2024.

Liang, J., Hu, D., and Feng, J. Do we really need to access the source data? source hypothesis transfer for unsupervised domain adaptation. In *International conference on machine learning*, pp. 6028–6039. PMLR, 2020.

Liang, J., He, R., and Tan, T. A comprehensive survey on test-time adaptation under distribution shifts. *International Journal of Computer Vision*, 133(1):31–64, 2025.

Lim, H., Kim, B., Choo, J., and Choi, S. Ttn: A domainshift aware batch normalization in test-time adaptation. In *11th International Conference on Learning Representations*, 2023.

Luo, X., Chen, K., Sun, P.-S. V., Tian, C. X., Basu, A., and Li, H. Space: Spike-aware consistency enhancement for test-time adaptation in spiking neural networks. *Advances in Neural Information Processing Systems*, 2025.

Ma, K., Tang, J., Guo, B., Dang, F., Liu, S., Zhu, Z., Wu, L., Fang, C., Chen, Y.-C., Yu, Z., et al. Surgeon: Memory-adaptive fully test-time adaptation via dynamic activation sparsity. In *Proceedings of the Computer Vision and Pattern Recognition Conference*, pp. 30514–30523, 2025.

Marsden, R. A., Döbler, M., and Yang, B. Universal test-time adaptation through weight ensembling, diversity weighting, and prior correction. In *Proceedings of the IEEE/CVF Winter Conference on Applications of Computer Vision*, pp. 2555–2565, 2024.

Mirza, M. J., Micorek, J., Possegger, H., and Bischof, H. The norm must go on: Dynamic unsupervised domain adaptation by normalization. In *Proceedings of the IEEE/CVF conference on computer vision and pattern recognition*, pp. 14765–14775, 2022.

Niu, S., Wu, J., Zhang, Y., Chen, Y., Zheng, S., Zhao, P., and Tan, M. Efficient test-time model adaptation without forgetting. In *International conference on machine learning*, pp. 16888–16905. PMLR, 2022.

Niu, S., Wu, J., Zhang, Y., Wen, Z., Chen, Y., Zhao, P., and Tan, M. Towards stable test-time adaptation in dynamic wild world. In *The Eleventh International Conference on Learning Representations*, 2023.

Niu, S., Miao, C., Chen, G., Wu, P., and Zhao, P. Test-time model adaptation with only forward passes. In *The International Conference on Machine Learning*, 2024.

Peng, X., Bai, Q., Xia, X., Huang, Z., Saenko, K., and Wang, B. Moment matching for multi-source domain adaptation. In *Proceedings of the IEEE/CVF international conference on computer vision*, pp. 1406–1415, 2019.

Piczak, K. J. Esc: Dataset for environmental sound classification. In *Proceedings of the 23rd ACM international conference on Multimedia*, pp. 1015–1018, 2015.

Qin, D., Leichner, C., Delakis, M., Fornoni, M., Luo, S., Yang, F., Wang, W., Banbury, C., Ye, C., Akin, B., et al. Mobilenetv4: universal models for the mobile ecosystem. In *European Conference on Computer Vision*, pp. 78–96. Springer, 2024.

Recht, B., Roelofs, R., Schmidt, L., and Shankar, V. Do imagenet classifiers generalize to imagenet? In *International conference on machine learning*, pp. 5389–5400. PMLR, 2019.

Russakovsky, O., Deng, J., Su, H., Krause, J., Satheesh, S., Ma, S., Huang, Z., Karpathy, A., Khosla, A., Bernstein, M., Berg, A. C., and Fei-Fei, L. ImageNet Large Scale Visual Recognition Challenge. *International Journal of Computer Vision (IJCV)*, 115(3):211–252, 2015. doi: 10.1007/s11263-015-0816-y.

Schneider, S., Rusak, E., Eck, L., Bringmann, O., Brendel, W., and Bethge, M. Improving robustness against common corruptions by covariate shift adaptation. *Advances in neural information processing systems*, 33: 11539–11551, 2020.

Shannon, C. E. A mathematical theory of communication. *The Bell system technical journal*, 27(3):379–423, 1948.

Shen, S., Yue, H., and Yang, J. Dec-adapter: Exploring efficient decoder-side adapter for bridging screen content and natural image compression. In *Proceedings of the IEEE/CVF International Conference on Computer Vision*, pp. 12887–12896, 2023.

Shen, Y., Gu, J., Tang, X., and Zhou, B. Interpreting the latent space of gans for semantic face editing. In *Proceedings of the IEEE/CVF conference on computer vision and pattern recognition*, pp. 9243–9252, 2020.

Song, J., Lee, J., Kweon, I. S., and Choi, S. Ecotta: Memory-efficient continual test-time adaptation via self-distilled regularization. In *Proceedings of the IEEE/CVF Conference on Computer Vision and Pattern Recognition*, pp. 11920–11929, 2023.

Sun, Y., Wang, X., Liu, Z., Miller, J., Efros, A., and Hardt, M. Test-time training with self-supervision for generalization under distribution shifts. In *International conference on machine learning*, pp. 9229–9248. PMLR, 2020.

Tan, M. and Le, Q. Efficientnet: Rethinking model scaling for convolutional neural networks. In *International conference on machine learning*, pp. 6105–6114. PMLR, 2019.

Vahdat, A., Kreis, K., and Kautz, J. Score-based generative modeling in latent space. *Advances in neural information processing systems*, 34:11287–11302, 2021.

Wang, D., Shelhamer, E., Liu, S., Olshausen, B., and Darrell, T. Tent: Fully test-time adaptation by entropy minimization. In *International Conference on Learning Representations*, 2021. URL <https://openreview.net/forum?id=uX13bZLkr3c>.

Wang, H., Ge, S., Lipton, Z., and Xing, E. P. Learning robust global representations by penalizing local predictive power. *Advances in neural information processing systems*, 32, 2019.

Wang, Q., Fink, O., Van Gool, L., and Dai, D. Continual test-time domain adaptation. In *Proceedings of the IEEE/CVF Conference on Computer Vision and Pattern Recognition*, pp. 7201–7211, 2022.

Warden, P. Speech commands: A dataset for limited-vocabulary speech recognition. *arXiv preprint arXiv:1804.03209*, 2018.

Yang, J., Luo, X., Ke, Y., Wang, Z., Shang, H., Dong, S., Fu, Z., Yang, X., Liu, H., and Basu, A. A 33.6–136.2-
tops/w nonlinear analog computing-in-memory macro for multi-bit lstm accelerator in 65-nm cmos. *IEEE Journal of Solid-State Circuits*, 2025.

Yang, X., Chen, X., Li, M., Wei, K., and Deng, C. A versatile framework for continual test-time domain adaptation: Balancing discriminability and generalizability. In *Proceedings of the IEEE/CVF Conference on Computer Vision and Pattern Recognition*, pp. 23731–23740, 2024.

Zhang, M., Levine, S., and Finn, C. Memo: Test time robustness via adaptation and augmentation. *Advances in neural information processing systems*, 35:38629–38642, 2022.

A. Covariance Matrix Adaptation Evolution Strategy

To enable single-instance TTA on resource-constrained edge devices and to avoid backpropagation, we adopt the Covariance Matrix Adaptation Evolution Strategy (CMA-ES) (Hansen, 2016) as our optimizer. CMA-ES is a gradient-free, population-based method for black-box optimization in continuous multi-dimensional spaces, making it a natural choice for our forward-only latent subspace search where only a small set of latent coordinates is updated.

At iteration t , CMA-ES maintains a multivariate Gaussian search distribution $\mathcal{N}(\mathbf{m}^{(t)}, (\sigma^{(t)})^2 \mathbf{C}^{(t)})$, where $\mathbf{m}^{(t)}$ is the mean, $\sigma^{(t)}$ is the step size, and $\mathbf{C}^{(t)}$ is the normalized covariance (shape) matrix. Throughout the paper, we denote the full covariance by $\Sigma^{(t)} = (\sigma^{(t)})^2 \mathbf{C}^{(t)}$. CMA-ES samples a population of candidates $\{\mathbf{p}_i^{(t)}\}_{i=1}^{\lambda}$ as

$$\mathbf{p}_i^{(t)} \sim \mathcal{N}(\mathbf{m}^{(t)}, (\sigma^{(t)})^2 \mathbf{C}^{(t)}) \Leftrightarrow \mathbf{p}_i^{(t)} = \mathbf{m}^{(t)} + \sigma^{(t)} \boldsymbol{\epsilon}_i, \boldsymbol{\epsilon}_i \sim \mathcal{N}(\mathbf{0}, \mathbf{C}^{(t)}). \quad (6)$$

Each candidate is evaluated by our fitness function, the output Shannon entropy $H(\mathbf{y})$. The mean $\mathbf{m}^{(t)}$ is then updated by a weighted recombination of the top-ranked candidates, while $\mathbf{C}^{(t)}$ (and $\sigma^{(t)}$) are adapted to reflect promising search directions and step sizes.

Beyond being gradient-free, CMA-ES is particularly compatible with our latent subspace coordinate search for two reasons. First, covariance adaptation exploits anisotropic structure in the subspace, improving sample efficiency. Second, by optimizing the expected fitness under its search distribution, CMA-ES implicitly performs a Gaussian smoothing of the entropy objective. Through the linear latent mapping, this corresponds to a rank- k smoothing in the original latent space with covariance $\mathbf{V}_k \Sigma^{(t)} \mathbf{V}_k^\top$ (Proposition 3.2). This distributional optimization makes entropy minimization less sensitive to local decision-boundary instabilities (e.g., noise-induced top-1 flips) without introducing auxiliary losses.

B. Proofs of Theoretical Justification

B.1. Proof of Proposition 3.1

Statement. For $\mathbf{z}_{adapted} = \mathbf{z}_t + \mathbf{V}_k \mathbf{p}$, $\|\mathbf{z}_{adapted} - \mathbf{z}^*\|^2 = \|\boldsymbol{\xi}_{\parallel} + \mathbf{V}_k \mathbf{p}\|^2 + \|\boldsymbol{\xi}_{\perp}\|^2$.

Proof. Let $\mathbf{z}_t = \mathbf{z}^* + \boldsymbol{\xi}$, and $\mathbf{V}_k \in \mathbb{R}^{D \times k}$ be full column-rank and span the chosen k -dimensional subspace. The orthogonal projector onto $\text{span}(\mathbf{V}_k)$ is

$$\mathbf{P} = \mathbf{V}_k (\mathbf{V}_k^\top \mathbf{V}_k)^{-1} \mathbf{V}_k^\top.$$

In particular, when \mathbf{V}_k has orthonormal columns ($\mathbf{V}_k^\top \mathbf{V}_k = \mathbf{I}_k$), this reduces to $\mathbf{P} = \mathbf{V}_k \mathbf{V}_k^\top$.

Decompose $\boldsymbol{\xi}$ into its components parallel and perpendicular to $\text{span}(\mathbf{V}_k)$ by

$$\boldsymbol{\xi}_{\parallel} := \mathbf{P} \boldsymbol{\xi}, \quad \boldsymbol{\xi}_{\perp} := (\mathbf{I} - \mathbf{P}) \boldsymbol{\xi}.$$

Then $\boldsymbol{\xi}_{\parallel} \in \text{span}(\mathbf{V}_k)$, and $\boldsymbol{\xi}_{\perp} \perp \text{span}(\mathbf{V}_k)$ because

$$\mathbf{V}_k^\top \boldsymbol{\xi}_{\perp} = \mathbf{V}_k^\top (\mathbf{I} - \mathbf{P}) \boldsymbol{\xi} = \mathbf{V}_k^\top \boldsymbol{\xi} - \mathbf{V}_k^\top \mathbf{V}_k \mathbf{V}_k^\top \boldsymbol{\xi} = \mathbf{V}_k^\top \boldsymbol{\xi} - \mathbf{I}_k \mathbf{V}_k^\top \boldsymbol{\xi} = \mathbf{0}.$$

Now

$$\mathbf{z}_{adapted} - \mathbf{z}^* = (\mathbf{z}^* + \boldsymbol{\xi} + \mathbf{V}_k \mathbf{p}) - \mathbf{z}^* = \boldsymbol{\xi}_{\parallel} + \boldsymbol{\xi}_{\perp} + \mathbf{V}_k \mathbf{p} = (\boldsymbol{\xi}_{\parallel} + \mathbf{V}_k \mathbf{p}) + \boldsymbol{\xi}_{\perp}.$$

Since $\boldsymbol{\xi}_{\parallel} + \mathbf{V}_k \mathbf{p} \in \text{span}(\mathbf{V}_k)$ and $\boldsymbol{\xi}_{\perp} \perp \text{span}(\mathbf{V}_k)$, we have $(\boldsymbol{\xi}_{\parallel} + \mathbf{V}_k \mathbf{p})^\top \boldsymbol{\xi}_{\perp} = 0$. Therefore,

$$\|\mathbf{z}_{adapted} - \mathbf{z}^*\|^2 = \|(\boldsymbol{\xi}_{\parallel} + \mathbf{V}_k \mathbf{p}) + \boldsymbol{\xi}_{\perp}\|^2 = \|\boldsymbol{\xi}_{\parallel} + \mathbf{V}_k \mathbf{p}\|^2 + \|\boldsymbol{\xi}_{\perp}\|^2,$$

where the cross term vanishes by orthogonality. This also implies the orthogonal component $\boldsymbol{\xi}_{\perp}$ cannot be altered by any choice of \mathbf{p} . \square

B.2. Proof of Proposition 3.2

Statement. Let $J(\mathbf{m}, \Sigma) = \mathbb{E}_{\mathbf{p} \sim \mathcal{N}(\mathbf{m}, \Sigma)} [\mathcal{L}(\mathbf{p})]$. Then $\nabla_{\mathbf{m}} J(\mathbf{m}, \Sigma) = \mathbb{E}_{\mathbf{p} \sim \mathcal{N}(\mathbf{m}, \Sigma)} [\mathcal{L}(\mathbf{p}) \Sigma^{-1} (\mathbf{p} - \mathbf{m})]$. Moreover, smoothing in \mathbf{p} induces a rank- k Gaussian smoothing in latent space with covariance $\mathbf{V}_k \Sigma \mathbf{V}_k^\top$.

Table 8. Performance of QELaTTA on ImageNet-C with ViT-Base model regarding **Accuracy** (%). QELaTTA-V2 (xby) indicates CMA-ES using x -bit fixed point with y -bit integer.

Method	Noise			Blur				Weather				Digital			Average Acc.	
	Gauss.	Shot	Impl.	Defoc.	Glass	Motion	Zoom	Snow	Frost	Fog	Brit.	Contr.	Elas.	Pix.	JPEG	
ELaTTA	58.77	59.66	59.50	49.30	36.08	55.35	46.34	65.21	66.40	67.66	80.21	35.96	47.61	69.55	69.68	57.82
QELaTTA-V1	59.41	60.15	60.09	49.86	36.48	55.94	46.70	65.60	66.74	60.90	80.46	34.55	47.72	69.83	70.01	57.63
QELaTTA-V2 (8b5)	56.16	57.11	56.93	47.17	35.14	53.60	44.76	63.18	63.94	67.60	78.37	33.03	46.26	67.48	67.49	55.88
QELaTTA-V2 (8b4)	56.75	57.75	57.35	47.63	35.32	53.99	45.12	63.60	64.39	68.34	78.66	33.71	46.51	67.83	67.88	56.32
QELaTTA-V2 (8b3)	56.73	57.61	57.42	47.63	35.35	53.90	45.04	63.49	64.35	68.07	78.65	33.16	46.53	67.75	67.77	56.23
QELaTTA-V2 (8b2)	56.64	57.59	57.37	47.55	35.37	53.99	45.08	63.52	64.28	67.76	78.56	33.41	46.49	67.72	67.81	56.21
QELaTTA-V2 (4b4)	55.06	55.88	55.62	45.53	34.41	52.50	43.96	62.39	61.66	64.82	77.59	33.29	45.46	66.48	66.54	54.75
QELaTTA-V2 (4b2)	55.41	56.35	56.15	46.56	34.78	52.93	44.24	62.44	62.85	65.84	77.82	32.10	45.78	66.76	66.72	55.12

Proof. **Smoothed objective.** By definition,

$$J(\mathbf{m}, \Sigma) = \int \mathcal{L}(\mathbf{p}) \mathcal{N}(\mathbf{p}; \mathbf{m}, \Sigma) d\mathbf{p}, \quad (7)$$

which is the Gaussian convolution (local averaging) of \mathcal{L} in \mathbf{p} -space.

Gradient with respect to \mathbf{m} . Under mild regularity conditions that allow differentiation under the integral sign,

$$\nabla_{\mathbf{m}} J(\mathbf{m}, \Sigma) = \int \mathcal{L}(\mathbf{p}) \nabla_{\mathbf{m}} \mathcal{N}(\mathbf{p}; \mathbf{m}, \Sigma) d\mathbf{p} \quad (8)$$

$$= \int \mathcal{L}(\mathbf{p}) \nabla_{\mathbf{m}} \log \mathcal{N}(\mathbf{p}; \mathbf{m}, \Sigma) \mathcal{N}(\mathbf{p}; \mathbf{m}, \Sigma) d\mathbf{p}. \quad (9)$$

Using the Gaussian score function $\nabla_{\mathbf{m}} \log \mathcal{N}(\mathbf{p}; \mathbf{m}, \Sigma) = \Sigma^{-1}(\mathbf{p} - \mathbf{m})$, we obtain

$$\nabla_{\mathbf{m}} J(\mathbf{m}, \Sigma) = \mathbb{E}_{\mathbf{p} \sim \mathcal{N}(\mathbf{m}, \Sigma)} [\mathcal{L}(\mathbf{p}) \Sigma^{-1}(\mathbf{p} - \mathbf{m})]. \quad (10)$$

Induced smoothing in latent space. Let $\mathbf{z}(\mathbf{p}) = \mathbf{z}_t + \mathbf{V}_k \mathbf{p}$. If $\mathbf{p} \sim \mathcal{N}(\mathbf{m}, \Sigma)$, then

$$\mathbf{z}(\mathbf{p}) \sim \mathcal{N}(\mathbf{z}_t + \mathbf{V}_k \mathbf{m}, \mathbf{V}_k \Sigma \mathbf{V}_k^\top). \quad (11)$$

Since $\mathbf{V}_k \Sigma \mathbf{V}_k^\top$ has rank at most k , the induced Gaussian smoothing in \mathbf{z} is restricted to $\text{span}(\mathbf{V}_k)$. \square

Remark (Implications for CMA-ES and decision flips). CMA-ES maintains $\mathbf{p} \sim \mathcal{N}(\mathbf{m}, \Sigma)$ and updates \mathbf{m} using ranked samples, which yields a stochastic, scale-adaptive descent direction for the neighborhood-averaged objective J . Optimizing J favors solutions that achieve low entropy not only at a single point but also in a local neighborhood. Near decision boundaries, predictions are highly sensitive and small perturbations can flip the top-1 class, which increases the variability of entropy in the neighborhood. By emphasizing neighborhood performance, the update becomes less sensitive to such flips and reduces the tendency of pointwise entropy minimization to reinforce an incorrect current prediction.

C. Quantization of ELaTTA

Scope. This section investigates quantized variants of ELaTTA (QELaTTA) as an extension to stress-test the optimization under low-precision arithmetic and to inform future hardware-algorithm co-design. Importantly, QELaTTA is *not required* for our ZYNQ-7020 proof-of-concept. The demo runs with the platform’s native 16-bit fixed-point arithmetic, whereas QELaTTA explores *more aggressive* quantization settings (e.g., 8/4-bit and 1-bit) and their accuracy-efficiency trade-offs.

Motivation. Low-precision arithmetic (e.g., fixed-point) is common in resource-limited edge deployments and can reduce memory and compute overhead. To further probe the efficiency limits of ELaTTA and highlight its potential for future hardware-algorithm co-design, we study whether ELaTTA’s optimization remains effective under *extreme* numerical constraints. Concretely, we introduce two exploratory quantized variants and evaluate their performance under different bit-width settings.

Quantized variants. Let \mathbf{p} denote the optimization target updated during TTA. The two variants are

Table 9. Performance of QELaTTA on ImageNet-V2/R/Sketch with ViT-Base model regarding **Accuracy (%)**. QELaTTA-V2 (xby) indicates CMA-ES using x -bit fixed point with y -bit integer.

Method	Accuracy (%)			
	V2	R	Sketch	Avg.
ELaTTA	78.15	65.29	47.73	63.72
QELaTTA-V1	77.46	63.31	46.79	62.52
QELaTTA-V2 (8b5)	76.94	62.02	46.33	61.76
QELaTTA-V2 (8b4)	77.21	62.06	46.37	61.88
QELaTTA-V2 (8b3)	76.86	61.45	45.99	61.43
QELaTTA-V2 (8b2)	76.26	60.42	45.39	60.69
QELaTTA-V2 (4b4)	75.17	57.70	44.65	59.17
QELaTTA-V2 (4b2)	75.46	59.42	44.88	59.92

Table 10. Performance of QELaTTA on GSC-C with LSTM model regarding **Accuracy (%)**. QELaTTA-V2 (xby) indicates CMA-ES using x -bit fixed point with y -bit integer.

SNR	Method	Animals		Natural		Human		Domestic		Urban		Average Acc.
		dog	cat	pouringwater	thunderstorm	cryingbaby	laughing	washingmachine	vacuumcleaner	carhorn	fireworks	
-10 dB	ELaTTA (QELaTTA-V1)	64.25	63.58	59.73	66.47	61.99	61.94	59.46	56.98	59.32	64.90	61.86
	QELaTTA-V2 (8b2)	63.70	62.65	57.71	66.63	60.56	60.74	57.09	55.03	58.37	63.42	60.59
	QELaTTA-V2 (8b1)	63.85	62.85	57.33	66.67	60.67	60.43	58.01	54.11	58.53	63.60	60.61
	QELaTTA-V2 (4b2)	63.65	63.17	57.26	66.65	60.64	60.51	58.05	53.87	58.68	63.66	60.61
	QELaTTA-V2 (4b1)	63.42	62.10	56.02	66.69	59.69	59.50	55.51	52.26	57.66	62.19	59.50
-15 dB	ELaTTA (QELaTTA-V1)	60.84	57.99	57.71	62.28	58.04	58.98	57.83	55.38	56.00	60.41	58.55
	QELaTTA-V2 (8b2)	59.66	55.90	54.82	62.14	56.39	56.97	55.80	53.22	54.51	58.29	56.77
	QELaTTA-V2 (8b1)	59.22	56.88	53.69	62.00	56.55	55.76	55.48	51.63	54.37	57.37	56.30
	QELaTTA-V2 (4b2)	59.26	56.85	53.77	61.98	56.59	55.79	55.40	51.53	54.41	57.09	56.27
	QELaTTA-V2 (4b1)	58.27	55.09	51.57	61.97	54.90	54.31	51.24	49.47	53.18	56.08	54.61
-20 dB	ELaTTA (QELaTTA-V1)	59.07	54.71	57.20	59.35	56.94	57.94	58.22	55.54	54.50	58.07	57.15
	QELaTTA-V2 (8b2)	56.98	51.06	53.86	59.36	55.39	54.59	56.62	53.18	52.25	55.90	54.92
	QELaTTA-V2 (8b1)	55.99	52.12	51.58	59.23	55.13	52.36	54.03	52.50	51.69	53.54	53.82
	QELaTTA-V2 (4b2)	56.07	51.97	51.78	59.05	55.23	52.51	53.90	52.42	51.79	53.60	53.83
	QELaTTA-V2 (4b1)	54.41	49.80	48.61	58.74	53.24	50.34	48.63	49.35	50.58	51.79	51.55

Definition C.1. QELaTTA-V1. After each iteration, we quantize \mathbf{p} into a *1-bit* representation, i.e., each element of \mathbf{p} can take only two values. From a hardware perspective, this reduces the optimization to controlling k binary switches, substantially lowering compute and memory cost, and minimizing the update overhead during single-instance TTA.

Definition C.2. QELaTTA-V2. Building on QELaTTA-V1, we further quantize the CMA-ES procedure by simulating it using *fixed-point* arithmetic (with configurable bit-widths), reducing reliance on high-precision floating-point support while aiming to preserve the effectiveness of the optimization dynamics.

Experimental results. Table 8, Table 9, and Table 10 report ELaTTA performance under various quantization configurations. For QELaTTA-V1, quantizing \mathbf{p} to 1-bit makes the update equivalent to toggling k binary switches, yielding a favorable accuracy–cost trade-off. It achieves an average accuracy of 57.63% and 62.52% on the ImageNet series, close to full-precision ELaTTA. For the KWS task, we fix $k=2$, in which case \mathbf{p} consists of two kinds of values. This can be regarded as natural 1-bit; therefore, ELaTTA reduces to QELaTTA-V1 in this setting.

For QELaTTA-V2, we replace floating-point CMA-ES with fixed-point arithmetic. In the IC task, QELaTTA-V2 (8b4) reaches 56.32% and 61.88% accuracy, indicating that 8-bit fixed-point precision is sufficient for effective optimization. For KWS, where the model is simpler, 4-bit QELaTTA-V2 already provides effective TTA. Overall, these results support the feasibility of ELaTTA on resource-limited edge devices, indicating that QELaTTA-V1 minimizes resource overhead, while QELaTTA-V2 improves compatibility with fixed-point hardware.

D. More Experimental Details

D.1. More Details on Dataset

ImageNet-C (Hendrycks & Dietterich, 2019) is a standardized benchmark for assessing the robustness of image classifiers to common distribution shifts. It applies 15 algorithmically generated, label-preserving corruptions to the 50,000 images in the ImageNet-1k validation set, each at five severity levels, yielding 75 corrupted test sets (3.75 million images). The corruptions span four categories, including noise (Gaussian, shot, impulse), blur (defocus, glass, motion, zoom), weather (snow, frost, fog, brightness), and digital artifacts (contrast, elastic transform, pixelate, JPEG compression). In our experiments, we specifically utilize severity level 5 for evaluation.

ImageNet-V2 (Recht et al., 2019) re-creates ImageNet-1k test sets to evaluate generalization under natural distribution shift. It replicates the original ImageNet data collection and annotation pipeline to curate new images for the same 1,000 classes, and provides three variants including matched-frequency, threshold-0.7, and top-images, each comprising 10,000 images (10 per class). The variants differ by selection criteria based on “selection frequency” (the fraction of annotators endorsing the target label). Matched-frequency reproduces the selection-frequency distribution of the original validation set. Threshold-0.7 retains images with selection frequency ≥ 0.7 . Top-images uses the highest-agreement images.

ImageNet-R (Renditions) (Hendrycks et al., 2021) is a benchmark for evaluating model robustness to non-photorealistic domain shifts. It comprises approximately 30,000 images collected from diverse artistic and abstract media such as sketches, cartoons, paintings, graffiti, embroidery, sculptures and origami, mapped to a 200-class subset of ImageNet-1k. The renditions are intended to be label-preserving while inducing substantial shifts in texture, color, and style.

ImageNet-Sketch (Wang et al., 2019) is a benchmark for evaluating robustness and shape bias under domain shift. It comprises approximately 50,000 black-and-white line drawings mapped to the 1,000 ImageNet-1k classes. The sketches are intended to be label-preserving while largely removing texture cues, thereby emphasizing contour and global shape.

DomainNet-126 (Peng et al., 2019) is a large-scale multi-source domain adaptation benchmark constructed from a 126-class subset of the original DomainNet dataset. It contains images from four heterogeneous domains including clipart, painting, real, and sketch, covering both natural photographs and various non-photorealistic styles. These domains exhibit substantial variations in texture, color, abstraction level, and drawing style, making DomainNet-126 a challenging testbed for studying domain generalization and adaptation under significant appearance shifts.

GSC-C is a controlled corruption benchmark for keyword spotting that simulates everyday acoustic interference by mixing Google Speech Commands (GSC; Warden (2018)) with real-world background noise from ESC-50 (Piczak, 2015). We consider five noise categories, which are Animals, Natural, Human, Domestic, and Urban. Within each, two representative soundscapes are selected, including dog, cat, pouring water, thunderstorm, crying baby, laughing, washing machine, vacuum cleaner, car horn, and fireworks. For each GSC utterance, we randomly sample a segment from an ESC-50 clip (to match the GSC duration) and additively mix it at diverse signal-to-noise ratios (SNRs), yielding multiple corrupted versions per utterance across SNR levels. Mixing is label-preserving and performed without time alignment beyond random cropping.

D.2. More Details on Backbone

Table 11. Five backbone models and their hidden size D (first dimension of the latent PC basis \mathbf{V}_k).

Model	ViT-Base	ResNet-50	EfficientNet-B0	MobileNet-V4	LSTM
D	768	2048	1280	1280	32

We use five backbone encoders: (1) ViT-Base (Dosovitskiy et al., 2021), (2) ResNet-50 (He et al., 2016), (3) EfficientNet-B0 (Tan & Le, 2019), (4) MobileNet-V4 (Qin et al., 2024), and (5) LSTM (Yang et al., 2025). Table 11 reports each model’s hidden size, i.e., the dimensionality D of the latent PC basis \mathbf{V}_k used throughout the paper.

D.3. More Ablation Studies

Performance under Continual TTA Settings. To demonstrate the practicality of ELaTTA in streaming scenarios, we further evaluate a *continual* protocol where adaptation proceeds along the test stream without per-sample reset. Importantly, our *strict* and *continual* modes share the same inference pipeline and objective; the only difference is how we initialize the latent coefficient for each new sample in Algorithm 1. Strict single-instance uses $\mathbf{m}^{(0)} \leftarrow \mathbf{0}$, whereas continual single-instance

Table 12. Performance comparison on ImageNet-C with ViT-Base model regarding **Accuracy (%)** under continual single-instance setting. The **bold** number indicates the best result.

Method	Memory (MB)	Time																		Average Acc.
		Noise		Blur			Weather			Digital										
Gauss.	Shot	Impl.	Defoc.	Glass	Motion	Zoom	Snow	Frost	Fog	Brit.	Contr.	Elas.	Pix.	JPEG						
No Adapt	-	55.34	56.23	56.01	46.48	34.78	52.87	44.20	62.39	62.66	65.56	77.70	32.04	45.73	66.72	66.67	55.03			
ROID	1345	0.10	0.08	0.08	0.08	0.08	0.08	0.08	0.08	0.08	0.08	0.08	0.08	0.08	0.08	0.08	0.08	0.08	0.08	0.08
Yang et al. (2024)	4033	3.86	6.68	1.82	0.13	9.16	8.10	3.77	0.82	0.34	0.14	79.24	0.10	0.21	73.60	70.95	17.26			
FOA	702	6.94	1.74	1.42	1.72	0.40	0.48	0.68	0.86	0.72	0.98	2.04	0.88	0.86	0.22	0.96	1.39			
ZOA	846	0.06	0.06	0.06	0.06	0.06	0.06	0.06	0.06	0.06	0.06	0.06	0.06	0.06	0.06	0.06	0.06	0.06	0.06	0.06
T3A	1128	55.18	56.72	56.00	38.88	32.96	50.96	42.82	60.14	60.18	64.22	76.48	40.24	43.12	66.60	68.48	54.20			
SAR	1288	59.08	60.52	59.36	45.52	57.26	58.56	57.12	62.74	66.66	68.68	78.78	6.68	67.16	72.40	71.56	59.47			
ELaTTA	696	61.78	62.40	62.98	51.82	39.50	57.74	47.44	68.92	68.52	68.72	80.80	31.74	56.20	70.30	67.94	59.79			

Table 13. Performance comparison on ImageNet-C with ViT-Base model regarding **Accuracy (%)** under continual batch setting. The **bold** number indicates the best result.

Method	Memory (MB)	Time																		Average Acc.
		Noise		Blur			Weather			Digital										
Gauss.	Shot	Impl.	Defoc.	Glass	Motion	Zoom	Snow	Frost	Fog	Brit.	Contr.	Elas.	Pix.	JPEG						
No Adapt	-	55.34	56.23	56.01	46.48	34.78	52.87	44.20	62.39	62.66	65.56	77.70	32.04	45.73	66.72	66.67	55.03			
ROID	10866	60.68	63.04	63.00	56.60	55.84	62.72	58.86	66.78	66.70	70.76	79.24	12.14	57.02	69.46	71.04	60.93			
Yang et al. (2024)	19489	58.52	63.92	64.46	50.34	40.66	56.58	44.94	67.62	68.42	66.48	77.74	39.54	51.66	68.46	69.70	59.27			
FOA	1300	57.14	61.62	61.96	51.98	42.78	57.48	54.08	65.98	68.44	65.60	79.48	62.78	52.20	70.32	72.20	61.60			
ZOA	1734	58.00	58.56	59.38	47.98	39.10	56.38	49.38	65.68	63.48	62.68	79.34	49.02	50.76	66.84	70.34	58.46			
T3A	6818	58.70	61.18	61.40	47.48	48.88	50.98	50.92	62.82	62.30	64.90	78.32	60.40	54.78	67.50	69.44	60.49			
SAR	1458	55.18	56.72	56.02	38.76	33.04	50.98	42.72	60.12	60.12	64.22	76.48	40.22	43.10	66.62	68.44	54.18			
BECoTTA	3340	61.82	62.52	62.27	51.64	38.10	58.16	48.65	67.79	68.82	36.77	82.20	30.69	49.38	71.99	72.11	57.53			
SURGEON	2124	60.43	60.95	62.88	50.39	36.66	56.52	47.35	68.32	67.32	69.61	80.91	32.93	57.94	70.42	70.53	59.54			
ELaTTA	1290	61.38	61.98	62.64	51.08	39.16	57.70	47.20	68.76	68.60	71.50	79.96	30.78	55.78	69.28	67.08	59.53			

warm-starts with the previous solution, i.e., $\mathbf{m}^{(0)} \leftarrow \mathbf{p}_{\text{prev}}$. This change introduces no additional trainable parameters and requires storing only one k -dimensional vector. To ensure a comprehensive comparison in continual settings, we additionally include recent methods designed for streaming adaptation, including ROIID (Marsden et al., 2024), ZOA (Deng et al., 2025), and Yang et al. (2024). We consider two settings.

1) Continual single-instance (Table 12). In this setting, many gradient-based TTA methods may suffer from error accumulation or catastrophic forgetting over long streams due to repeated parameter updates. In contrast, ELaTTA keeps the backbone fixed and only optimizes a low-dimensional \mathbf{p} , which substantially limits drift. Moreover, continual warm-starting explains why continual can outperform strict single-instance (e.g., 59.79 vs. 57.82 in our IC results). We initialize each sample’s CMA-ES search with the previous solution \mathbf{p}_{prev} , which improves sample efficiency within each domain segment. When the stream shifts across domains, \mathbf{p}_{prev} may become suboptimal, but it only serves as an initialization. \mathbf{p} is still re-optimized per sample, and the low-dimensional, subspace-constrained search allows CMA-ES to rapidly move away from a poor starting point without accumulating irreversible drift in the backbone. As a result, ELaTTA achieves state-of-the-art accuracy while also requiring the lowest peak memory among all compared methods.

2) Continual batch (Table 13). For batch-level streaming (batch size = 64), we apply a shared latent coefficient vector \mathbf{p} within each batch and warm-start the next batch using the previous batch solution. Although this shared adjustment is less granular than per-sample optimization, ELaTTA remains highly competitive in accuracy and retains its advantage of a minimal peak memory footprint.

Effect of Source Sample Size N and Offline Nature. First, we clarify that ELaTTA computes the latent basis \mathbf{V}_k entirely **offline**. Similar to how BN statistics are frozen after training, \mathbf{V}_k is pre-computed and stored (requiring negligible storage, $\approx 0.01\%$ of the model size for ViT-Base), ensuring no source data is needed during TTA.

Regarding the sensitivity to sample size, we extend our ablation to a wide range ($N \in [20, 50000]$) as shown in Table 14 and detailed Table 15. Contrary to the intuition that more data always yields better bases, we observe a *non-monotonic* behavior. Remarkably, extremely small sample sizes (e.g., $N = 20 \sim 50$) achieve an average accuracy of 59.14%, which is comparable to, or even superior to, utilizing the full validation set (57.82% at $N = 50$ k). However, performance dips significantly in the medium regime ($N \approx 1$ k), hitting a local minimum of 51.5%. This phenomenon is most pronounced in corruptions like *Fog*, where accuracy starts high at small N (72.8%), collapses at $N = 1$ k (7.3%), and eventually recovers at $N = 50$ k (67.7%).

Table 14. Performance comparison on ImageNet-C with ViT-Base model using various N to obtain \mathbf{V}_k regarding average **Accuracy** (%) and **Loss** value. The **bold** number indicates the best result.

N	50k	40k	30k	20k	10k	5k	3k	1k	500	100	50	30	20
Acc.	57.82	57.69	57.28	56.89	56.53	55.94	53.41	51.52	54.75	58.66	59.08	59.14	59.13
Loss	2.33	2.45	2.52	2.59	2.43	2.62	2.77	2.75	2.38	2.20	2.23	2.25	2.19

Table 15. Performance comparison on ImageNet-C with ViT-Base model using various N to obtain \mathbf{V}_k regarding detailed **Accuracy** (%).

N	Noise			Blur			Weather			Digital			Average Acc.			
	Gauss.	Shot	Impl.	Defoc.	Glass	Motion	Zoom	Snow	Frost	Fog	Brit.	Contr.	Elas.	Pix.	JPEG	
20	60.69	60.50	61.24	50.07	37.76	56.36	47.39	65.71	67.23	72.79	81.07	35.76	48.54	70.50	71.36	59.13
30	60.69	60.41	61.24	50.27	37.80	56.39	47.40	65.61	67.05	72.61	81.01	36.37	48.44	70.53	71.29	59.14
50	60.83	60.53	61.39	50.33	37.73	56.50	47.39	65.89	67.07	71.65	80.81	35.66	48.60	70.47	71.31	59.08
100	60.65	60.59	61.28	50.06	37.57	56.32	47.39	65.30	66.96	68.88	81.00	33.64	48.50	70.40	71.30	58.66
500	60.30	59.67	60.66	49.87	37.16	56.06	47.14	65.27	66.03	16.79	80.56	33.17	47.87	70.03	70.71	54.75
1000	59.22	59.11	59.82	48.99	37.19	55.46	46.76	64.73	65.31	7.26	80.21	1.02	48.10	69.28	70.31	51.52
3000	59.03	59.11	59.68	49.24	37.19	55.44	46.85	64.66	65.04	29.36	79.79	8.32	47.94	69.22	70.23	53.41
50k	58.77	59.66	59.50	49.30	36.08	55.35	46.34	65.21	66.40	67.66	80.21	35.96	47.61	69.55	69.68	57.82

We attribute this behavior to the purity of the subspace directions. With very few samples, the subspace captures only the most dominant, class-discriminative directions. As N increases to the medium regime, the subspace begins to include less stable directions (noise) that vary across samples, which may mislead the unsupervised objective. When N further increases, these unstable directions are statistically averaged out, restoring performance. This hypothesis is strongly corroborated by the interaction between N and the subspace dimension k (Table 16). For small N , performance is robust and insensitive to k , indicating the absence of noisy directions. In contrast, for medium N , accuracy drops sharply as k increases, confirming that a larger dimension introduces more unstable components in this regime.

These findings underscore the practicality of ELaTTA, which remains highly effective even when only a handful of source samples are available.

Effect of gradient free optimizer. To validate the choice of CMA-ES, we compared it against several representative gradient-free baselines within the same latent subspace, including Uniform Random Search, (1+1)-Evolution Strategy ((1+1)-ES), and Zeroth-Order SGD (ZO-SGD). As shown in Table 17, Uniform Random Search yields high instability and negligible gains due to the lack of directional guidance. While (1+1)-ES offers some improvement, it converges slowly, requiring significantly more iterations (e.g., 14 vs. 8 evaluations per sample on ViT) to achieve weaker TTA performance. We also observed that ZO-SGD suffers from high variance in gradient estimation within the single-instance regime, making it difficult to stabilize without extensive hyperparameter tuning. In contrast, CMA-ES consistently delivers reliable accuracy improvements with fewer evaluations and lower variance. Beyond algorithmic performance, CMA-ES is chosen for its practicality. It is fully gradient-free (relying solely on forward passes) and benefits from mature implementations in both Python and C/C++, facilitating seamless integration into edge-device runtimes. Thus, we adopt CMA-ES not as an algorithmic novelty, but as the most stable and hardware-friendly tool for our specific TTA formulation.

Performance on in-distribution dataset. We further evaluate ELaTTA’s performance on in-distribution data (*i.e.*, the source test dataset). As shown in Table 18, our method achieves significant performance improvements across various models. This result highlights two key points. (1) The notable performance gain demonstrates that our method effectively mitigates catastrophic forgetting, as it even enhances the model’s performance on the original data distribution. (2) The improvement can be attributed to the inherent distribution shift between the source test data and the training data. Our ELaTTA framework adjusts the latent representations of test samples to be more compactly aligned within the defined principal subspace, which reduces uncertainty and enables the model to produce more confident predictions.

Performance on DomainNet-126. To further assess the robustness of ELaTTA under rigorous conditions beyond synthetic corruptions (e.g., ImageNet-C), we extend our evaluation to DomainNet-126 (Peng et al., 2019). Unlike corruption benchmarks that primarily introduce texture or noise degradations while preserving object geometry, DomainNet features significant semantic and stylistic variations across four distinct domains (Real, Sketch, Clipart, and Painting), presenting a substantial challenge for adaptation methods.

As shown in Table 19, ELaTTA exhibits superior generalization capabilities across these severe distribution shifts. In the online batch setting, ELaTTA remains highly competitive with state-of-the-art methods. However, the advantage of ELaTTA

Table 16. Accuracy (%) on ImageNet-C with ViT-Base using diverse N and k .

$N \setminus k$	4	8	16	32
30	58.03	59.09	59.14	59.15
1k	54.63	56.25	51.52	48.74
5k	55.39	56.61	57.82	57.90

Table 17. Performance comparison on ImageNet-C with ViT-Base model using different gradient-free optimizers regarding Accuracy (%).

Optimizer	Noise			Blur			Weather			Digital			Average Acc.			
	Gauss.	Shot	Impl.	Defoc.	Glass	Motion	Zoom	Snow	Frost	Fog	Brit.	Contr.	Elas.	Pix.	JPEG	
Uniform Random Search	43.86	46.68	41.82	40.13	49.16	48.10	43.77	40.82	40.34	40.14	63.24	40.10	40.21	63.60	60.95	46.86
(1+1) ES	56.10	56.93	56.79	47.20	35.17	53.49	44.82	62.95	63.59	66.94	78.10	33.11	46.22	67.26	67.23	55.73
ZO-SGD	55.06	55.88	52.62	45.53	34.41	52.50	43.96	62.39	59.66	64.82	77.59	21.29	45.46	66.48	66.54	53.61
CMA-ES (Our Choice)	58.77	59.66	59.50	49.30	36.08	55.35	46.34	65.21	66.40	67.66	80.21	35.96	47.61	69.55	69.68	57.82

becomes most pronounced in the single-instance setting. Given DomainNet’s extreme diversity and large domain gaps, existing baselines are prone to error accumulation and catastrophic forgetting when processing samples sequentially. In contrast, ELaTTA effectively mitigates these issues, maintaining stable and robust performance. These results confirm that ELaTTA is not only effective against local corruptions but also resilient to complex structural domain shifts.

Table 18. Performance on in-distribution dataset with different models regarding **Accuracy (%)**.

Model	Vit-Base	ResNet-50	EfficientNet-B0	MobileNet-V4
No Adapt	85.16	70.74	78.53	71.04
ELaTTA	87.05	76.71	85.31	79.91
Improvement	+1.89	+5.97	+6.78	+8.87

 Table 19. Performance Comparison on DomainNet-126 with ResNet-50 model regarding **Accuracy (%)**. **BS** stands for batch size.

(a) Painting as Source Domain

Method	Real	Sketch	Clipart	Avg.
No Adapt	74.84	49.70	53.26	59.27
SAR (BS=64)	73.58	53.96	53.50	60.35
ROID (BS=64)	75.04	57.30	57.24	63.19
SAR (BS=1)	6.42	4.24	3.22	4.63
ROID (BS=1)	0.48	0.16	0.16	0.27
MEMO (BS=1)	40.38	17.82	25.42	27.87
ELaTTA (BS=64)	78.24	53.74	55.50	62.49
ELaTTA (BS=1)	76.08	52.94	54.22	61.08

(b) Clipart as Source Domain

Method	Real	Sketch	Clipart	Avg.
No Adapt	46.16	60.50	43.84	50.17
SAR (BS=64)	48.80	64.36	47.34	53.50
ROID (BS=64)	51.24	64.64	49.14	55.01
SAR (BS=1)	4.98	5.80	4.38	5.05
ROID (BS=1)	0.16	0.48	0.30	0.31
MEMO (BS=1)	40.38	15.48	27.92	18.77
ELaTTA (BS=64)	47.24	63.24	46.08	52.19
ELaTTA (BS=1)	47.20	62.44	44.74	51.46

(c) Real as Source Domain

Method	Real	Sketch	Clipart	Avg.
No Adapt	48.48	54.88	59.32	54.23
SAR (BS=64)	57.56	58.98	67.92	61.49
ROID (BS=64)	58.76	61.44	68.58	62.93
SAR (BS=1)	4.78	4.50	5.26	4.85
ROID (BS=1)	0.30	0.16	0.48	0.31
MEMO (BS=1)	13.92	26.00	21.68	20.53
ELaTTA (BS=64)	56.52	61.32	64.46	60.77
ELaTTA (BS=1)	54.44	59.50	63.50	59.15

(d) Sketch as Source Domain

Method	Real	Sketch	Clipart	Avg.
No Adapt	55.62	61.88	47.84	55.11
SAR (BS=64)	54.36	62.90	48.40	55.22
ROID (BS=64)	57.48	65.18	52.66	58.44
SAR (BS=1)	3.74	4.66	3.58	3.99
ROID (BS=1)	0.16	0.30	0.16	0.21
MEMO (BS=1)	40.38	26.12	22.92	21.63
ELaTTA (BS=64)	56.40	63.28	49.82	56.50
ELaTTA (BS=1)	56.50	63.12	49.16	56.26